Materials Today Bio 31 (2025) 101450

Contents lists available at ScienceDirect

Materials Today Bio

journal homepage: www.journals.elsevier.com/materials-today-bio

In-vivo and ex-vivo evaluation of bio-inspired structures fabricated via PBF-LB for biomedical applications

Miguel Araya [a,b,*], Antti Järvenpää [b], Timo Rautio [b], Rafael Vindas [c], Roberto Estrada [c], Mylène de Ruijter [d], Teodolito Guillén [a]

[a] Bio-inspired Processes and Materials Research Group, Instituto Tecnológico de Costa Rica, Cartago, 30101, Costa Rica
[b] Future Manufacturing Technologies Research Group, University of Oulu, Oulu, 90014, Finland
[c] School of Veterinary Medicine, Universidad Nacional de Costa Rica, Heredia, 40104, Costa Rica
[d] Department of Orthopaedics, University Medical Center Utrecht, Utrecht, 3584, CX, the Netherlands

ARTICLE INFO

Keywords:
Powder bed fusion-laser beam (PBF-LB)
Ti64 lattice structures
Bio-inspired materials
Mechanical properties
Biocompatibility
Osseointegration
Biomedical implants

ABSTRACT

Titanium-based lattice structures have gained significant attention in biomedical engineering due to their potential to mimic bone-like behavior and improve implant performance. This study evaluates the performance of bio-inspired Ti64 TPMS Gyroyd and Stochastic lattice structures fabricated via Powder Bed Fusion-Laser Beam (PBF-LB), focusing on their in-vivo and ex-vivo mechanical and biological responses for biomedical applications. Utilizing an SLM 280 HL printer, samples exhibited notable geometric accuracy essential for mechanical integrity. The study highlights significant mechanical properties and geometric precision improvements achieved through chemical etching. Mechanical characterization revealed that the as-built Gyroid lattice had the highest elastic modulus (3.64 GPa) and yield strength (200.65 MPa), which improved post-etching (3.62 GPa and 219.35 MPa, respectively). The Stochastic lattice demonstrated lower yield strength values post-etching (169.81 MPa). In-vivo analyses in horse models, both structures demonstrated excellent biocompatibility and osseointegration with no adverse inflammatory responses. Ex-vivo push-out tests showed that the chemically etched Gyroid structure achieved the highest resistance to push-out force (1645.407 N) and most significant displacement (2.754 mm), indicating superior energy absorption (4920.425 mJ). These findings underscore the critical influence of microstructural design and surface treatments on implant functionality, offering novel insights into improving biomedical implant performance through lattice architecture and post-processing.

1. Introduction

In the growing field of biomaterials, the pursuit of optimizing implant designs for enhanced biomechanical compatibility and improved osseointegration continues to challenge researchers and clinicians alike. Traditional prosthetic designs often struggle to meet the complex demands of biocompatibility and mechanical stability, prompting the exploration of bio-inspired architectures. This study introduces two distinct structures: Triply Periodic Minimal Surface (TPMS) Gyroid and Stochastic Voronoi, both designed implicitly and manufactured using Powder Bed Fusion-Laser Beam (PBF-LB) Selective Laser Melting (SLM) technology, recognized for its precision in creating intricate geometries necessary for biomimetic applications.

The use of solid and porous metallic implants, particularly those made from Ti alloys, is considered a highly effective strategy in the field of biomedical engineering for bone replacement [1–3]. These materials are favored due to their structural and compositional properties that closely mimic the mechanics of natural bone. Ti and its alloys are commonly employed in biomedical implants because of their remarkable mechanical strength, robust corrosion resistance, and outstanding biocompatibility [4–8].

Biomimetic principles have significantly pushed the boundaries in material design for biomedical applications, particularly through the adoption of architectures that emulate natural biological structures. The use of TPMS and Stochastic structures has shown promising potential in fostering improved cellular responses and achieving mechanical

This article is part of a special issue entitled: Surface & Interface published in Materials Today Bio.

* Corresponding author. Bio-inspired Processes and Materials Research Group, Instituto Tecnológico de Costa Rica, Cartago, 30101, Costa Rica.miaraya@itcr.ac.cr
E-mail addresses: miaraya@itcr.ac.cr (M. Araya), antti.jarvenpaa@oulu.fi (A. Järvenpää), timo.rautio@oulu.fi (T. Rautio), rafael.vindas.bolanos@una.cr (R. Vindas), roberto.estrada.mcdermott@una.cr (R. Estrada), m.deruijter@umcutrecht.nl (M. de Ruijter), tguillen@itcr.ac.cr (T. Guillén).

https://doi.org/10.1016/j.mtbio.2025.101450
Received 19 August 2024; Received in revised form 28 October 2024; Accepted 3 January 2025
Available online 7 January 2025

stability. These innovative structures are increasingly recognized for their ability to optimize material distribution while maintaining an optimal balance between weight and strength, research has consistently shown that TPMS [9–15] and Stochastic [16–19] structures possess excellent mechanical and morphological properties.

Recent advancements in additive manufacturing, especially PBF-LB SLM technology, have revolutionized the production of complex implant geometries, previously deemed unachievable [20–23]. Such technologies facilitate the creation of patient-specific implants that not only fit anatomically but also feature tailored properties essential for optimal osseointegration and biomechanical performance [24–28]. Despite these advances, challenges such as surface roughness and micro-structural integrity persist, often necessitating additional post-processing steps to refine the implants for enhanced functional integration with biological tissues. The interaction between biomaterials and the body can lead to integration or chronic inflammation, largely influenced by the material's surface, which is the initial contact point with the body. This contact influences the healing and long-term success of implants [2]. Surface characteristics such as chemical composition and topography are crucial in bone-contact implants, affecting interactions like ion and biomolecule adsorption and the formation of biologically active layers, which are essential for compatibility with various cell types, including macrophages and osteoblasts [29]. Therefore, the interface between the implant and tissue is critical to the success of orthopedic implants, highlighting the importance of tissue compatibility.

Surface treatments are essential for optimizing performance in the practical application of titanium and its alloys, particularly in biomedical applications, as they enhance biocompatibility, wear resistance, and corrosion resistance, addressing issues such as poor chemical bonding, vulnerability to wear, and instability of protective layers in the challenging environment of the human body [2]. Chemical surface treatment stands out due to its straightforward procedure, adaptability to diverse shapes, minimal dependency on external factors, and consistently superior outcomes, significantly enhancing the surface quality and functionality of the metals [15,30].

This paper takes a novel approach by employing large animal models, specifically horses [31], in its in-vivo studies to simulate the clinical outcomes of human applications better. Large animal models are pivotal in orthopedic research due to their physiological and anatomical similarities to humans, particularly in bone healing processes and biomechanical loads [32–34]. The use of horses provides a more relevant assessment of biomechanical compatibility and osseointegration in conditions that closely mimic those in human orthopedic care. This approach not only enhances the translational relevance of the research but also offers a more robust evaluation of the performance and safety of bio-inspired implant designs under realistic physiological conditions.

This research extends the current discourse on the practical application of bio-inspired designs in clinical settings by providing a comparative analysis of the TPMS Gyroid and Stochastic Voronoi structures. It assesses their performance both mechanically and biologically after manufacturing and post-processing treatments aimed at improving surface characteristics for osseointegration.

2. Materials and methods

This section outlines the comprehensive methodologies employed for the design, manufacturing, post-processing, mechanical characterization, in-vivo experimental study, and subsequent analyses of open-cell lattice structures for biomedical applications. The investigation comprises the fabrication and assessment of two distinct lattice structures, followed by their surface treatment, mechanical testing, and in-vivo evaluation in an equine model. Further, the study extends to include post-operative monitoring and advanced microscopy analyses to evaluate the effects of the manufacturing and treatment processes on the structures' properties.

2.1. Design and manufacturing

Two open-cell lattice structures were evaluated: a walled triply periodic minimal surface (TPMS) gyroid structure governed by a specific mathematical equation allowing for the manipulation of unit cell size and porosity through variables "a" and "t" [35] and a stochastic Voronoi volume lattice generated by distributing points randomly within a designated space. These structures epitomize two principal lattice classifications: mathematically defined surfaces (TPMS gyroid) and beam-like element (stochastic) configurations [10].

$$\theta(x,y,z)_{Gyroid} = \sin\left(\frac{2\pi}{a}x\right)cos\left(\frac{2\pi}{a}y\right) + \sin\left(\frac{2\pi}{a}y\right)cos\left(\frac{2\pi}{a}z\right) + sin\left(\frac{2\pi}{a}z\right)cos\left(\frac{2\pi}{a}x\right) = t \quad (1)$$

The digital design of these lattices was executed using the implicit modeling capabilities of nTopology software (nTopology, New York, USA), facilitating a compact and efficient representation of three-dimensional geometries through mathematical functions. A target relative density of 0.3 was established based on the research team's preliminary static and dynamic assessments to ensure consistency across tests and structure comparability. This density was achieved by setting the wall/strut thickness to 0.250 μm and finely controlling two main variables: the unit cell size for the TPMS gyroid and the averaged spacing between random points for the stochastic lattice. Mechanical properties were evaluated through compressive testing of eight cylindrical specimens (12 mm diameter, 18 mm height with 1 mm top and bottom plates). The in-vivo evaluation involved the implantation of eight cylindrical specimens, each of 11 mm diameter with two lattice structures of 10 mm high, capped with a 1 mm top plate, specifically designed for this investigation. Fig. 1 shows graphically the design parameters of the structures and the samples.

Fabrication was realized via Powder Bed Fusion-Laser Beam (PBF-LB) Additive Manufacturing, employing a Selective Laser Melting (SLM) 280 HL 3D printer (SLM Solutions, Lübeck, Germany) and Ti-6Al-4V ELI (Grade 23) Titanium powder. This material, characterized by spherical particles of approximately 30 μm diameter and a density of 4.43 g/cm^3, was processed under conditions to achieve optimal part density and microstructural integrity. The main fabrication parameters used were: layer thickness of 0.03 mm, hatching tolerance of 0.1 mm, spacing of 0.12 mm, laser power of 500 W for contours and 300 W for internal hatches, and specific fill patterns ("Stripes" for external areas and "Chessboard" for internal volumes).

2.2. Surface treatment

Post-manufacturing, the specimens were subjected to one of two surface conditions. The initial group underwent a basic cleaning procedure (as-built condition), while the second group was chemically etched. Cleaning involved dual ultrasonic baths, first in distilled water and subsequently in ethanol, using a Cole Parmer 8892 ultrasonic cleaner. After cleaning, etching was performed using a solution of 70 %

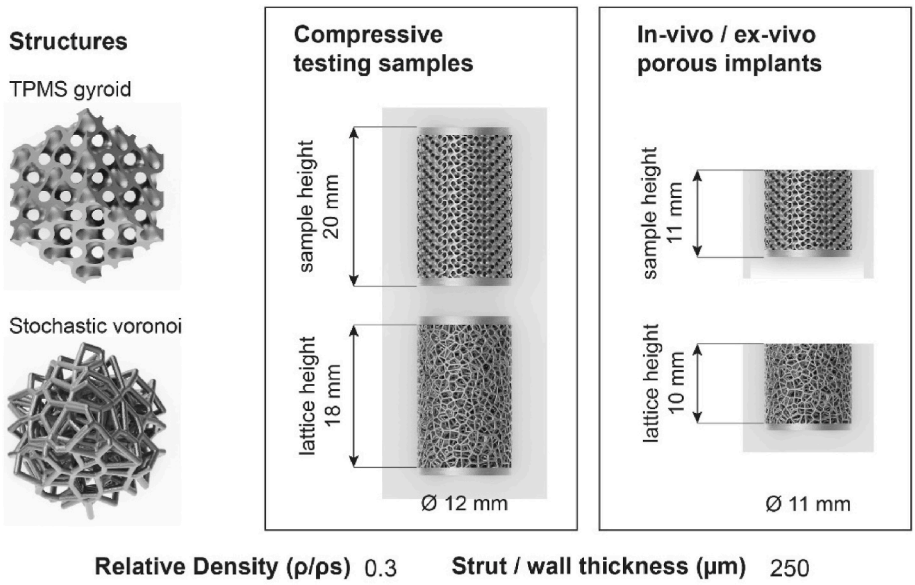

Fig. 1. Experimental design parameters of the samples.

ammonium hydroxide (NH4OH) and 30 % hydrogen peroxide (H2O2). This etching solution, used for titanium alloys, has been shown to improve surface characteristics by enhancing micro-roughness and removing micro-defects, which is beneficial for osseointegration and mechanical performance [36–38]. The ultrasonic bath settings were set to keep a temperature of 50 °C for 1 h during the etching process.

2.3. Surface roughness analysis method

Surface roughness analysis was conducted to characterize the topographical features of Ti64 Gyroid and Stochastic lattice structures in their as-built (AB) and chemically etched (CE) conditions. Surface roughness parameters, including average roughness (Ra), root mean square roughness (Rq), and average maximum height (Rz), were evaluated using a Zeta-20 profilometer from Zeta Instruments with a 50x lens. Ten distinct regions were measured per sample, and data were collected for each parameter. The roughness values were recorded as each sample condition's mean and standard deviation (SD).

2.4. Mechanical characterization

Testing adhered to ISO 13314 standards, employing a 10^{-2} s^{-1} compression strain rate, and was performed using a Tinius Olsen Universal Testing Machine equipped with a 50 KN load cell, from which stress-strain curves were derived. These curves facilitated the calculation of critical mechanical properties, including elastic modulus (E) and yield strength (σ_y), providing insights into the structural performance of the lattice designs under compressive loads.

2.5. In-vivo experimental study

The ethical and animal welfare committee and the National University of Costa Rica Veterinary School council approved the detailed protocol and study (UNA-EMV-CBBA-ACUE-001-2023/UNA-CO-EMV-ACUE-055-2023). Two healthy Criollo breed horses, males, free from lameness and devoid of clinical or radiographic signs of acute or chronic injuries, were selected as subjects for the implantation study. One horse weighed 338 kg and was 8 years old (H1), and the other weighed 340 kg and was 12 years old (H2). At the beginning of the study, they were housed in individual box stalls and were fed a standard maintenance diet comprising 2 kg of concentrates daily, supplemented with hay and water ad libitum. In the tubers coxae of each horse, both types of scaffolds were implanted randomly assigned to each side, resulting in two structures implanted on each side of the tuber coxa, totaling eight samples across both subjects.

The implantation surgical protocol commenced with intravenous (IV) premedication using xylazine (0.7 mg/kg; Chinfield, Argentina), followed by the placement of a 12G jugular venous catheter and administration of flunixin intravenously (1.1 mg/kg, Weizur, Argentina); gentamicin (6.6 mg/kg, Quimtia, Perú) IV and procaine penicillin (15000 IU/kg., Aranda, México) intramuscularly. Anesthesia induction and maintenance were achieved in the standing animal using IV Xilacine in continuous rate infusion (CRI) 0.7 mg/kg/h and butorphanol, Holliday, Argentina, 0.02 mg/kg. Local anesthesia was achieved by injecting a 10 ml mixture of lidocaine 2 %, Faryvet, Costa Rica (2/3) and bupivacaine, Lab. Sanderson, Costa Rica (1/3) in 10 ml around the incision site. Two precise vertical incisions, approximately 3 cm in length, were made through the skin and subcutaneous tissue over the tuber coxae by a board-certified equine surgeon (SC), exposing the underlying bone structure for implantation (one incision was made cranial and one caudal along each tuber coxae with about 7 cm between them). A cylindrical defect (11 mm diameter by 10 mm depth) was then created that was exactly perpendicular to the bony surface using a stop-controlled power drill. Prior to the press-fit implantation of the scaffolds (n = 8), each defect site was thoroughly flushed with saline (Baxter, Chile). Post-implantation, the incision sites were closed in two layers: the subcutis with polyglycolic acid 0, Atramat, México, and the skin with nylon 0, Atramat, México. Fig. 2 shows the surgical protocol.

2.6. Post-operative procedure

Following surgery, the animals were administered antibiotics and nonsteroidal anti-inflammatory drugs (NSAIDs) to mitigate infection risks and manage inflammation consisting of procaine penicillin (15,000 IU/kg, intramuscularly daily, Aranda, México) and gentamicin (6.6 mg/kg intravenously daily, Quimtia, Perú) for three days. Flunixin (1.1 mg/kg IV; Weizur, Argentina) was provided for four days to alleviate the pain. Clinical monitoring was conducted daily, focusing on vital parameters such as rectal temperature, heart rate, and respiratory rate, alongside evaluations of the animals' stance, demeanor, and overall appearance. The skin stitches were removed the third week after surgery, after which the horses were turned out to pasture for free exercise.

Eight months after the surgeries, the horses were humanely euthanized with a combination of xylazine (1 mg/kg IV, Chinfield, Argentina)

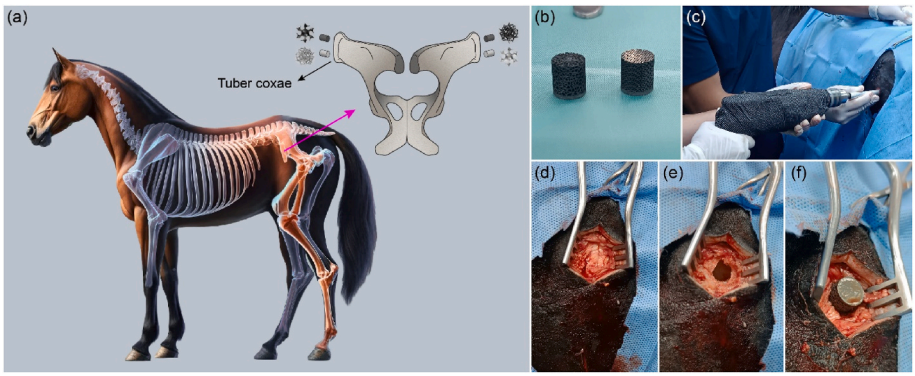

Fig. 2. Surgical procedures. Protocol schematic representation (a), implant samples in sterilized area (b), use of stop-controlled drill (c), incision in subcutaneous tissue (d), cylindrical defect of 11 mm diameter by 10 mm depth (e), and implant press-fit insertion (f).

and ketamine (2.2 mg/kg, respectively, Agrovetmarket, Perú) to induce a profound state of anesthesia, followed by a lethal dose of an oversaturated magnesium sulfate (200 g/L) and chloral hydrate (200 g/L) solution. Death was confirmed by the cessation of breathing, lack of corneal reflex, and the absence of the ictus cordis. Following euthanasia, the implanted sites were exposed through the careful dissection of the skin and subcutaneous tissues over the tuber coxae. Tissue blocks containing the implants were then meticulously excised for further analysis.

Six extracted samples were designated for biomechanical push-out testing to assess the integration strength between the implant and surrounding bone tissue. These bone-implant samples were harvested and stored in vessels containing saline solution (0.9 % sodium chloride) to simulate physiological conditions prior to biomechanical testing.

2.7. Push-out biomechanical assessment

A biomechanical push-out assessment was conducted after the in-vivo study period to evaluate the integration strength between the implanted lattice structures and the surrounding bone tissue. This analysis was conducted 2–3 h post-explantation to ensure the bone remained as fresh as possible and to minimize the loss of biological information regarding the osseointegration of the bone in the implants. The blocks of tissue with the implants were cleaned and cut, leaving flat surfaces parallel to the top and bottom of the implants (Fig. 3 (d)), and were securely mounted in a push-out accessory, which was itself aligned to an MTS Bionix universal testing machine equipped with a 2.5 KN load cell as shown in Fig. 3. The alignment was carefully adjusted to guarantee a parallel force transmission from the machine to the implant during testing. The assessment was performed at a constant strain rate of 3 mm/min until the implant was fully extricated from the bone, allowing for the precise measurement of the force required to dislodge the implant.

2.8. Scanning electron microscopy

The implants extracted from the push-out tests were cleaned with water using an ultrasonic cleaner for 2 h. Subsequently, the samples were treated with isopropyl alcohol (IPA) in an ultrasonic cleaner for 1 h, followed by drying with compressed air. This cleaning cycle in IPA, ultrasonic treatment, and air drying was repeated five times. This procedure ensured the removal of all organic materials adhered to the implants and bone. Then, Scanning Electron Microscopy (SEM) analysis was conducted, utilizing a JEOL JSM-6010LA SEM at an operating voltage of 20 kV, to examine the microstructure and surface morphology of the lattice specimens in their as-built and etched states, with a particular focus on assessing osseointegration This analysis was performed to identify and verify the effects of the manufacturing process and surface treatments on the materials' characteristics and bone growth. Backscattered electron composition (BEC) was used to analyze the bone-metal interface.

3. Results and discussion

3.1. Design and manufacturing

Utilizing the SLM 280 HL printer, samples were fabricated via PBF-LB process. These structures exhibited the anticipated geometric accuracy and structural connectivity, critical for mechanical withstand. Fig. 4 depicts the surface morphology of both as-built and etched conditions. Notable manufacturing-related defects, such as the staircase effect and surface roughness, were observed, which is characteristic of the PBF-LB technique due to its inherent layer-by-layer fabrication

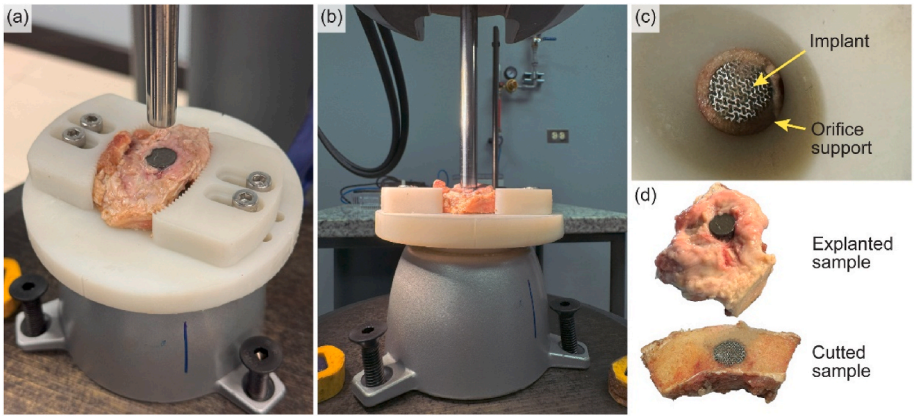

Fig. 3. Push-out accessory with a sample (a). Frontal view (b). View from beneath the specimen's support (c). Sample cut preparation before test (d).

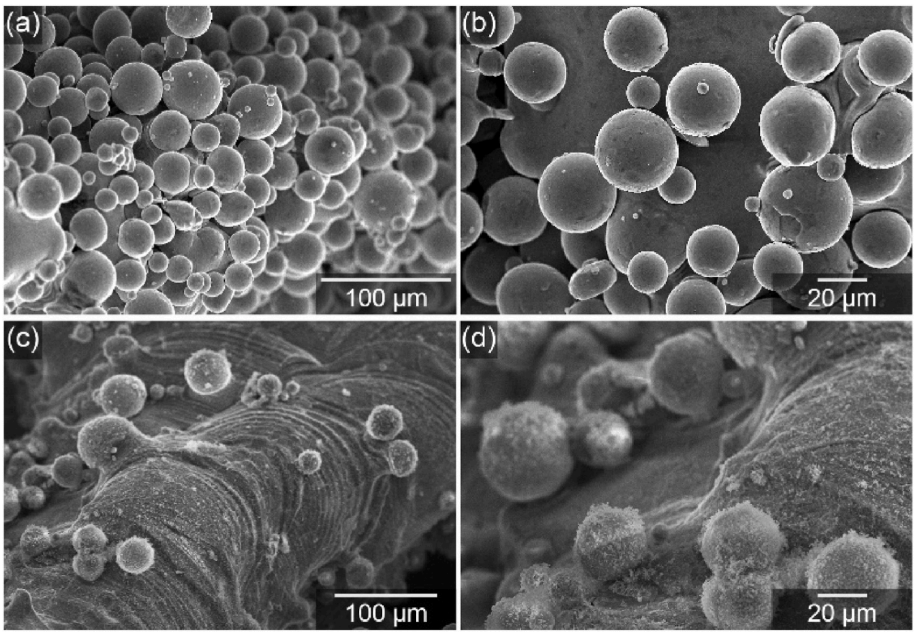

Fig. 4. SEM micrographs of the chemical etching effect. As built condition at 250x (a) and 700x (b). Etching treatment at 250x (c) and 700x (d).

method [12]. The surface roughness, primarily resulting from the adherence of partially melted powder particles, was exacerbated by the staircase effect, contributing to the overall texture [5,16,39,40]. Fig. 4 (a) and (b) highlight the rough surface texture in the as-built samples, particularly on the struts. In contrast, as shown in recent studies [36–38], the etching treatment has proven effective for titanium alloys, significantly smoothing the strut surfaces and potentially enhancing fatigue performance while maintaining biocompatibility and osseointegration capabilities [41]. The chemical etching process was applied to enhance the formation of a titanium dioxide (TiO_2) layer on the implant surface, which improves biocompatibility by promoting better bone cell attachment. This modification supports long-term implant stability by increasing bioactivity at the bone-implant interface. The ultrasonic cleaning step further refines the surface by removing residual particles from the additive manufacturing process, which could otherwise interfere with osseointegration or lead to inflammatory responses. These morphological changes align with the enhancements documented in previous research, underscoring their effectiveness in improving mechanical properties [42,43] and osseointegration [44].

Table 1 summarizes the Ra, Rq, and Rz results for the factor's combination of structures and treatment conditions. The surface roughness analysis revealed distinct differences in roughness parameters based on the lattice structure type and the post-processing condition. The analysis avoided geometric influences; for example, flat areas or regions distant from strut intersections were consistently used. The Gyroid structure exhibited higher surface roughness values across all parameters in the as-built (AB) condition than the Stochastic structure. Specifically, the Ra value for the as-built Gyroid was 10.09 μm, significantly higher than the Stochastic structure at 6.66 μm. Similarly, the Rq and Rz values were also elevated for the Gyroid in its as-built state, indicating a more pronounced surface texture.

Table 1
Surface roughness results.

Structure	Condition	Ra mean (μm)	Ra SD	Rq mean (μm)	Rq SD	Rz mean (μm)	Rz SD
Gyroid	AB	10.09	0.79	12.29	0.82	20.9	6.39
Gyroid	CE	5.14	1.8	6.54	1.98	12.57	4.49
Stochastic	AB	6.66	1.53	8.57	2.24	18.66	5.72
Stochastic	CE	4.48	3.14	5.58	3.44	12.94	10.32

Chemical etching (CE) had a pronounced effect in reducing the surface roughness of both structures. The Ra decreased to 5.14 μm post-etching for the Gyroid structure, while the Stochastic structure reduced to 4.48 μm. The decrease in roughness was also evident in the Rq and Rz parameters. After chemical etching, the Gyroid Rz value dropped from 20.9 μm to 12.57 μm, and the Stochastic structure saw a similar reduction from 18.66 μm to 12.94 μm. These findings demonstrate the efficacy of chemical etching in smoothing the surface topography of both lattice structures. The differential effect of chemical etching on the two structures highlights the importance of considering lattice geometry when selecting post-processing treatments. While both structures benefitted from reduced roughness, the Gyroid lattice showed a more significant relative reduction in roughness values, indicating that the etching process might be more effective for more geometrically complex designs. Fig. 5 shows the 3D images of roughness analysis before and after chemical etching.

3.2. Mechanical characterization

The elastic modulus and yield strength of Ti64 lattice samples exhibit variations attributed to their different lattice designs and post-processing treatments, as summarized in Fig. 6 and Table 2. The as-built Gyroid lattice (GAB) demonstrated the highest elastic modulus at 3.64 GPa, closely followed by the chemically etched Gyroid (GE) with 3.62 GPa. The Stochastic structures had lower elastic moduli, with the as-built Stochastic (SAB) lattice at 3.43 GPa and the chemically etched Stochastic (SE) lattice showing the lowest at 3.30 GPa. Similarly, the Gyroid lattices outperformed the Stochastic lattices in yield strength, with the chemically etched Gyroid (GE) achieving a significantly higher yield strength of 219.35 MPa compared to the as-built Gyroid (GAB) at 200.65 MPa. Conversely, yield strength decreased in the Stochastic lattices post-etching, with the as-built Stochastic (SAB) at 189.42 MPa and the chemically etched Stochastic (SE) at 169.81 MPa.

These variations in mechanical properties are likely due to the differences in the microstructure and residual stresses induced by the specific lattice designs and their post-processing. The organized and interconnected strut network of the Gyroid design contributes to better homogeneous stress distribution [45,46] and increased stiffness compared to the more randomized Stochastic lattice. Chemical etching

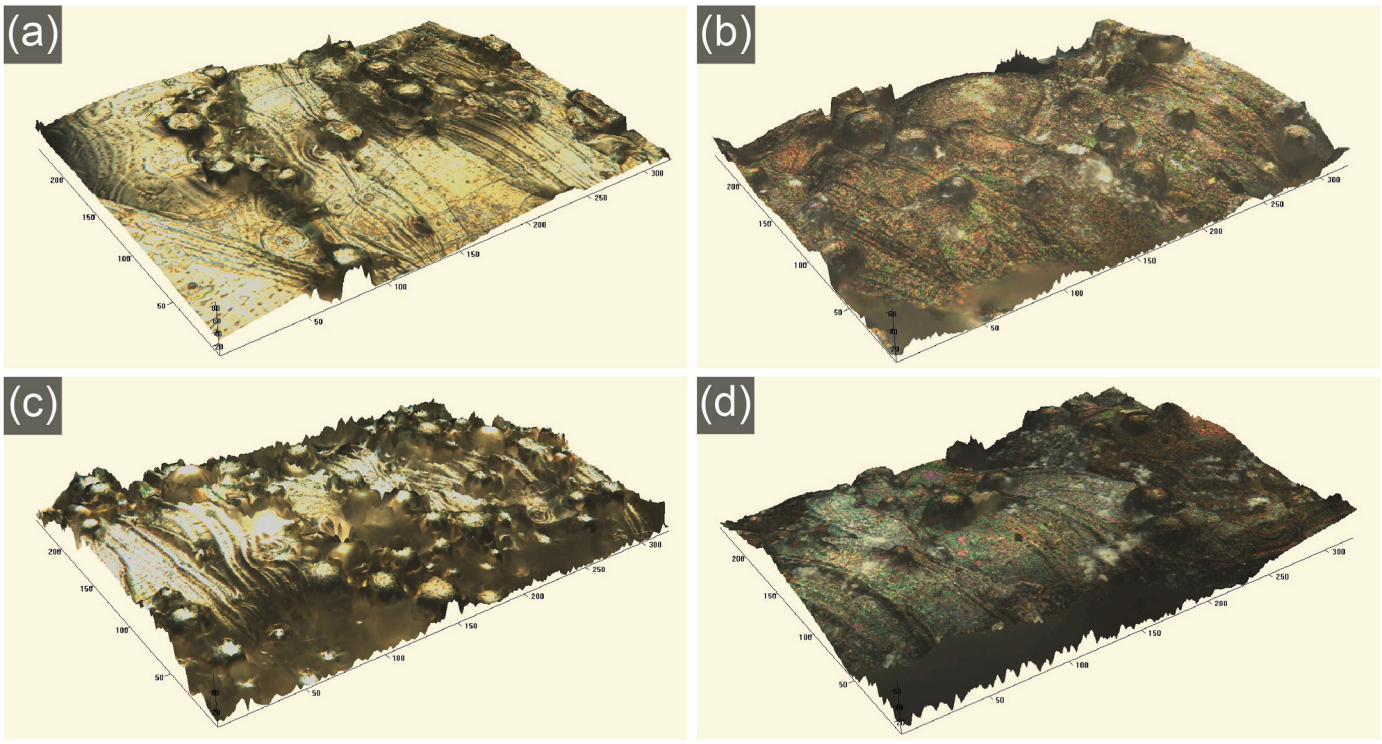

Fig. 5. 3D images of roughness analysis for gyroid as built (a), gyroid with etching (b), stochastic as built (c), and stochastic with etching (d).

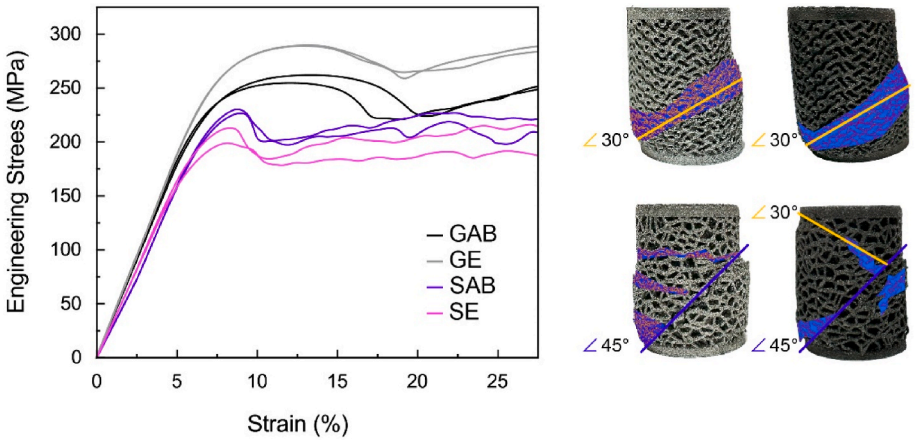

Fig. 6. Mechanical characterization - Compressive stress-strain curve (left). Examination of the compressive samples' failure mechanisms and deformation mode (right).

Table 2
Compressive mechanical characterization results.

Sample	Elastic Modulus (GPa)	Yield Strength (MPa)
GAB	3.64	200.65
GE	3.62	219.35
SAB	3.43	189.42
SE	3.30	169.81

generally improved the yield strength of the Gyroid lattice while reducing that of the Stochastic lattice, likely due to a reduction in strut thickness and the introduction of micro-defects during the etching process, adversely affecting the less organized Stochastic structure.

Fig. 6 illustrates distinct failure modes and deformation patterns, with both structures developing shear bands. The Gyroid structure formed a shear band angled at approximately 30° to the loading axis, while the Stochastic structure displayed a steeper shear band at 45°, consistent with deformation modes commonly reported in lattices produced by PBF-LB manufacturing [47,48]. Throughout the initial compression, the TPMS Gyroid and Stochastic structures exhibited buckling within the linear elastic regime, primarily localized in the middle of their struts or walls. As compression progressed, a plateau regime indicating the gradual collapse of the lattice was observed. This behavior varied between the structures; collapse in the TPMS Gyroid initiated at the sample's center, maintaining the initial shear band angle of about 30°. In contrast, the Stochastic structures began collapsing from the top down until a 45° shear band appeared. The deformation of the lattice structures under load was characterized by three distinct phases [49–51] as shown in Fig. 6 (left): (i) a linear elastic phase, where deformation occurred through the bending of cell edges or stretching of cell faces; (ii) a stress plateau phase, indicative of progressive cell failure via elastic buckling and plastic deformation; and (iii) a densification

phase, marked by the total collapse of the cells leading to compression between cell edges and faces.

Adjacent to the shear bands, distinct changes in the lattice structures under load were observed, as highlighted in Fig. 6 (right). The Gyroid structure showed regions of structural condensation near the shear bands, indicating material densification in response to compressive stress. Meanwhile, the Stochastic structure exhibited more frequent strut breakage, especially in the middle of struts, suggesting a difference in failure mechanisms.

3.3. Evaluation of implants during in-vivo test

After eight months, the surgical incisions healed without complications, and no local inflammatory reactions (heat, swelling, tenderness) or signs of pain or discomfort were observed at any time. Likewise, the animals did not experience any detectable pain or lameness during the postoperative, rehabilitation, or other periods of the experiment. Clinical and blood parameters remained within the normal physiologic limits. Fig. 7 shows the X-ray images of the first week after implantation and the final week before the explantation of the samples. The radiographic evaluations showed a lack of adverse reactions in adjacent bone tissues at the week of explantation (week 36); these results highlight the titanium alloy implants' excellent biocompatibility combined with the interconnectivity of the pores in the material, suggesting their suitability for integration without negative inflammatory responses and promoting bone ingrowth [52,53]. Implant displacement was observed as movement from initial positions, as highlighted in Fig. 7 (e,f,g, and h). This movement may result from osteoconduction, with new bone growth possibly exerting forces on the implants. The porous structure of the lattice likely supports this by acting as a scaffold that facilitates bone ingrowth and maturation, potentially altering implant positioning. This behavior underscores the dynamic interaction between bone development and the implants, further supported by the known benefits of titanium alloys in enhancing osteointegration through vascularization and bone ingrowth.

3.4. Ex-vivo biomechanical test

The ex-vivo push-out biomechanical testing assessed the stability and integration of Ti64 lattice implants in horse bone tissues under different conditions and designs. The data highlight the push-out force, displacement at push-out, and the strain energy density or absorbed energy by the samples during testing, as presented in Table 3 and graphically shown in Fig. 8.

Table 3
Ex-vivo push-out biomechanical results.

Sample	Push-out force (N)	Push-out displacement (mm)	Strain Energy Density/ Absorbed energy (mJ)
GAB-H1	1356.860	2.280	4920.425
GAB-H2	1234.633	1.574	3485.107
GE-H2	1645.407	2.754	4462.468
SAB-H1	1412.147	1.800	3398.129
SAB-H2	1124.962	1.768	3084.130
SE-H1	1042.042	2.316	2869.950

The highest resistance to push-out force was observed in the GE-H2 sample, which recorded a force of 1645.407 N. This was followed by the GAB-H1 with 1356.860 N, indicating robust mechanical interlocking and osseointegration. The lowest resistance was found in the SE-H1 sample, demonstrating a force of 1042.042 N, which is not a negligible value. GE-H2 exhibited the highest push-out force and the greatest displacement at 2.754 mm, suggesting a high degree of energy absorption before failure, which correlates with a more ductile interfacial integration. Conversely, GAB-H2 showed the least displacement at 1.574 mm, potentially indicating a stiffer interface or lesser energy absorption capacity. The absorbed energy during the push-out test was highest in GAB-H1 at 4920.425 mJ, illustrating that the as-built Gyroid structure in H1 could dissipate substantial energy, reflecting good bone embedding and energy absorption characteristics. SE-H1 recorded the lowest energy absorption at 2869.950 mJ.

The results demonstrate that the Gyroid structures, especially when chemically etched, enhance biomechanical interlocking and energy absorption capabilities compared to Stochastic Voronoi structures, similar to the findings reported by Kovác et al. [54]. This could be

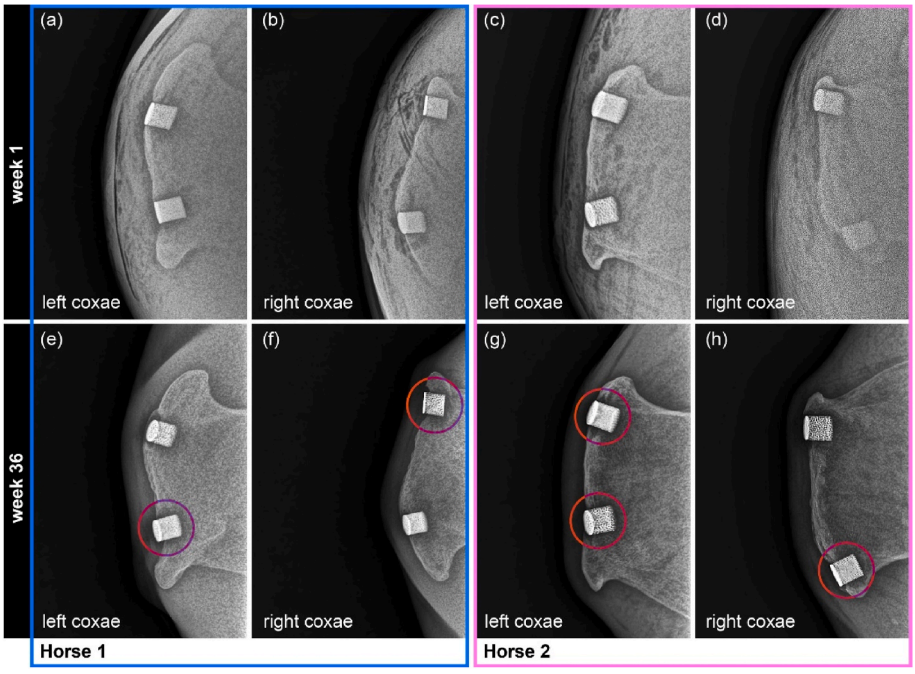

Fig. 7. X-ray images after implantation (a) and prior explantation of the samples (b).

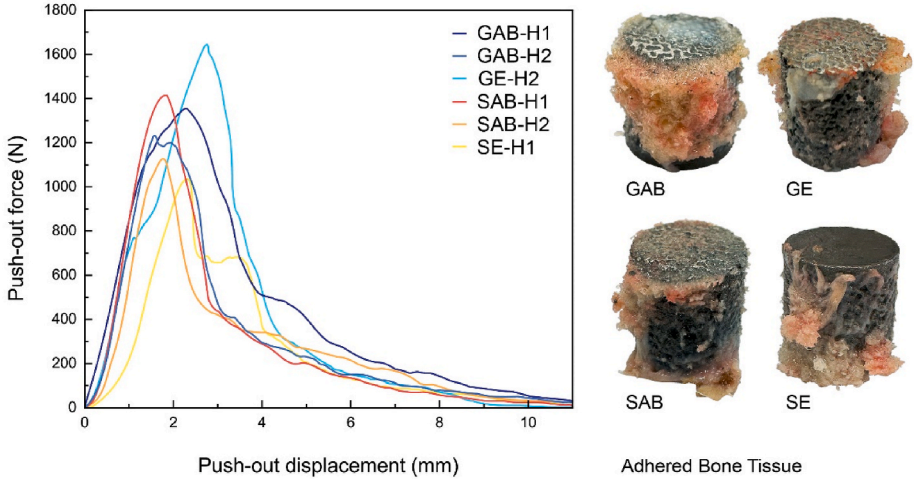

Fig. 8. Biomechanical testing. Force-Displacement Curve During Push-Out Test (Left). Specimens Post-Explantation with Adhered Bone Tissue (Right).

attributed to the more organized lattice architecture of the Gyroid design, which may provide better mechanical stability and stress distribution upon force application. Chemical etching appears to enhance the biomechanical performance of the Gyroid structures significantly, as evidenced by the highest push-out force and displacement in GE-H2. This treatment might have improved the micro-roughness and surface area for bone ingrowth, thus providing better mechanical anchorage and energy absorption capabilities [15,30]. The variability in displacement and absorbed energy across samples highlights differences in material behavior under load, which can be crucial for predicting the long-term success of implants. Samples that exhibited higher displacement and absorbed energy before failure (like GE-H2 and GAB-H1) are indicative of more resilient interfaces that can better accommodate physiological loads without failure.

Fig. 8 (right) displays some extracted samples with bone tissue encasing the metallic implants. Notably, this tissue remained attached to the samples following the push-out test. Despite applying high forces during the push-out tests, the fact that bone tissue remained adhered to the extracted samples indicates strong osseointegration and mechanical interlocking. The retention of bone tissue on the implant surfaces after exposure to significant mechanical loads highlights the mechanical stability and the robust biological fixation achieved by the implants. Such adherence is crucial, as it reflects the ability of the implant to withstand physiological stresses while maintaining its structural integrity and supportive role within the bone structure, and it is indicative of effective load transfer between the bone and the implant.

Fig. 9 outlines the methodological framework for SEM and BEC analysis following the ex-vivo evaluation. Initially, the SEM technique was utilized to investigate the interaction of bone tissue enveloping the implant with the intricate lattice structures. Subsequently, the samples were longitudinally sectioned to facilitate a detailed BEC analysis of bone ingrowth within the implants.

The SEM micrographs in Figs. 10 and 11 show the metal implant prominently enveloped by new bone formation in both the Gyroid and Stochastic structures, respectively. The bone tissue displayed robust integration, almost filling the internal voids of the implant structures, demonstrating effective osseointegration and cellular proliferation.

Our results, using horse tuber coxae implants, differ from those observed in a rabbit femoral condyle study [55] with comparable implant size, relative density, and pore size but a non-stochastic periodic structure. This study reported that only 50 % of the pore space in Ti-6Al-4V scaffolds was occupied by new bone by the ninth week, indicating restricted osteoinductive properties. These findings underscore the importance of structural design and animal model selection in assessing the osteoinductive properties of Ti-6Al-4V scaffolds and highlight that extended in-vivo studies could significantly enhance our understanding of osseointegration and bone tissue growth, potentially inspiring new avenues of research and clinical applications [32].

The SEM images also captured the interaction between bone tissue and unmelted Ti64 spheres, a characteristic feature of the PBF-LB process. This interaction is critical as it indicates a high level of microstructural adherence and cellular activity, with bone tissue surrounding these spheres, enhancing mechanical interlocking and biological fixation, as can be observed in Fig. 10 (a, b, e) and Fig. 11(a and b,d). The SEM micrographs in Figs. 10 (b) and Fig. 11(b–e) show the rupture of bone tissue resulting from the push-out test in samples. This rupture

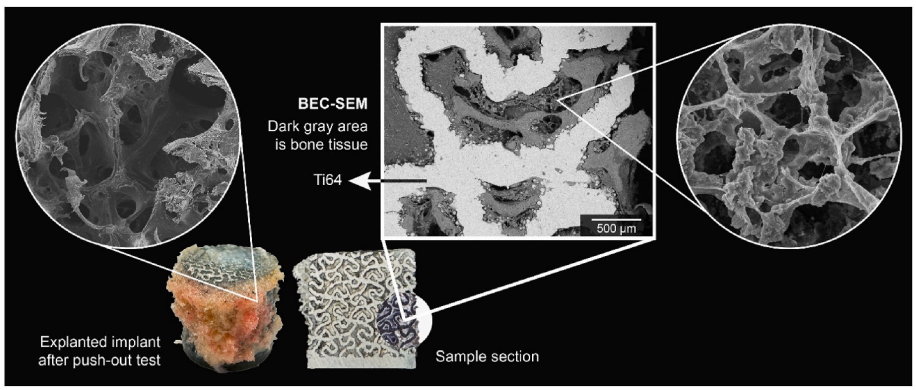

Fig. 9. Implant–bone interface.

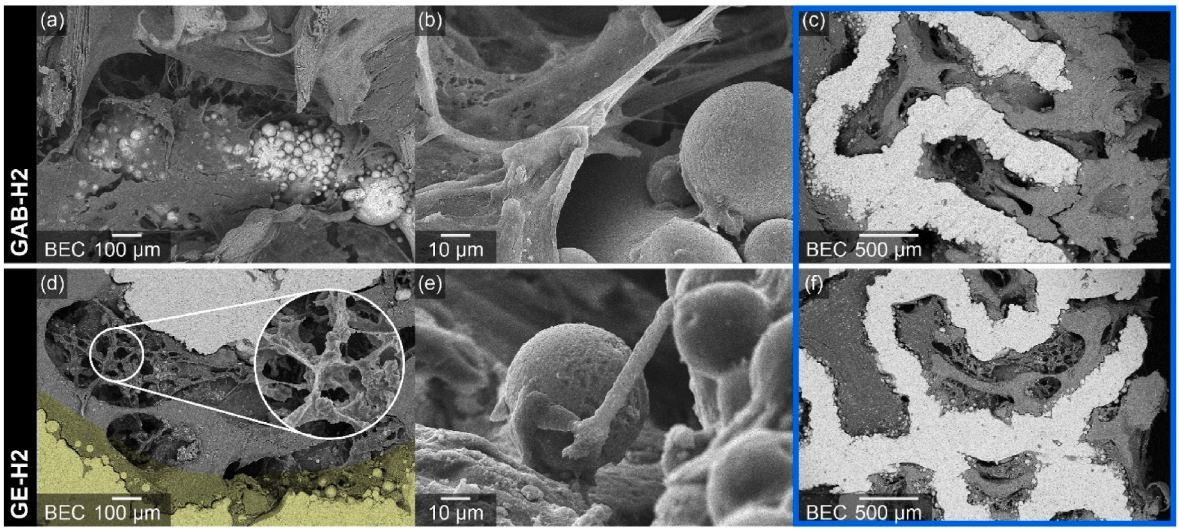

Fig. 10. SEM BEC micrographs of the osseointegration within the Gyroid implants.

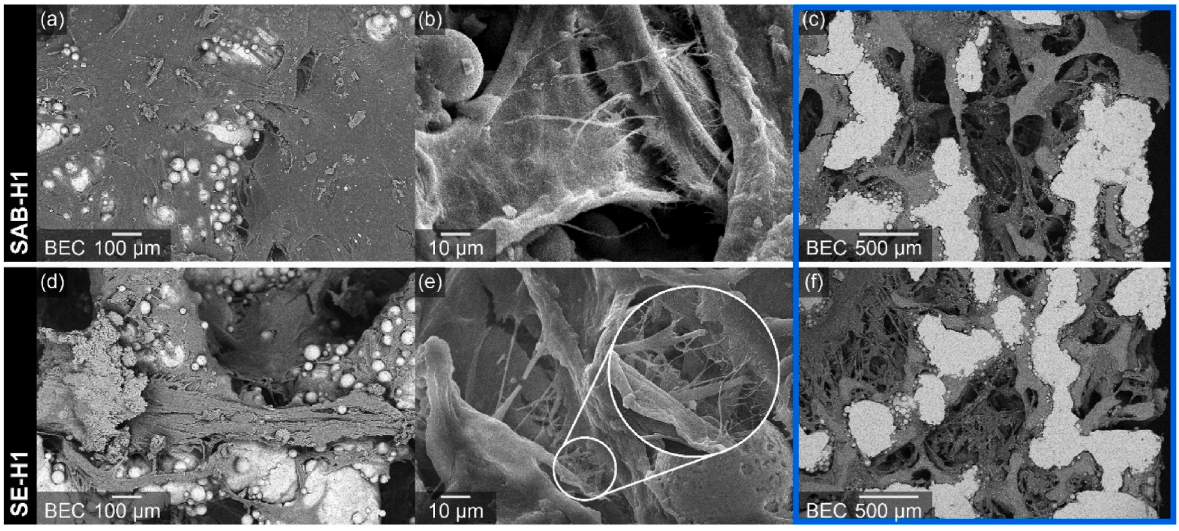

Fig. 11. SEM BEC micrographs of the osseointegration within the Stochastic implants.

appears as torn tissue, indicative of the mechanical stress exerted during testing.

The application of BEC imaging provided enhanced contrast at the bone-metal interface, allowing for detailed visualization of osseointegration and the interaction effects between the manufacturing process, surface treatments, and biological integration. The BEC images of the samples' cross-section presented in Fig. 10(c–f) and Fig. 11(c–f) highlight regions where bone tissue grew within the Ti64. Here, gray-scale differentiation indicates mature bone integration around the white-hued implant structures.

The observed osseointegration within both TPMS Gyroid and Stochastic Voronoi structures suggests that the lattice design is pivotal in promoting bone growth and vascularization. The open architecture of these lattices facilitates not only bone ingrowth but also vascular proliferation [56], which is crucial for sustaining newly formed bone tissue and enhancing the structural stability of the implant. Chemical etching of the lattice structures did not impede bone tissue growth; rather, it may have enhanced the micro-roughness of the implant surface, potentially promoting better cellular attachment and proliferation. This finding is consistent with previous research indicating that surface topography is a determinant factor in osteogenic response and integration. The substantial bone growth filling the implants' pores and internal spaces across all samples indicates excellent osseointegration. Such performance is typically attributed to good pore interconnectivity, which supports bone ingrowth and effective vascularization, which is essential for the nutritional support of the bone tissue.

4. Conclusions

This study successfully demonstrates the in-vivo and ex-vivo performance of bio-inspired Ti64 lattice structures fabricated using the PBF-LB technique, focusing on their biomechanical and osseointegration capabilities in horse bone tissue. The geometric precision and surface modifications achieved through chemical etching significantly enhance mechanical properties, especially in Gyroid structures, as evidenced by increased yield strength and improved stress distribution, leading to superior biomechanical interlocking.

Our findings highlight the pivotal role of lattice design in the implants' biomechanical performance and biological integration. The organized strut network of Gyroid lattices provides greater mechanical resilience and more uniform bone ingrowth compared to Stochastic lattices, suggesting that the architectural design of the lattice plays a

critical role in the osteogenic response and the implant's long-term stability. Additionally, surface modifications from chemical etching reduced micro-defects and enhanced micro-roughness. The in-vivo results corroborate the implants' excellent biocompatibility and integration capabilities, with no adverse reactions observed post-implantation. These findings support the potential of these bio-inspired materials for biomedical applications.

The research underscores the importance of integrating advanced manufacturing techniques with thoughtful design considerations to optimize the mechanical and biological performance of biomedical implants. The comparative analysis between Gyroid and Stochastic structures provides valuable insights into the tailored application of bio-inspired materials, paving the way for future innovations in the field of implantable biomedical devices.

Future work will expand upon these findings through detailed microCT and histological analyses of bone-implant interfaces, along with additional in-vivo and ex-vivo tests across larger sample sizes. Further mechanical testing will provide a comprehensive assessment under various loading conditions, ultimately refining the design and surface characteristics for enhanced clinical success.

CRediT authorship contribution statement

Miguel Araya: Writing – original draft, Visualization, Validation, Supervision, Software, Methodology, Investigation, Formal analysis, Conceptualization. **Antti Järvenpää:** Writing – review & editing, Supervision, Resources, Project administration, Investigation, Funding acquisition, Conceptualization. **Timo Rautio:** Writing – review & editing, Project administration, Investigation, Conceptualization. **Rafael Vindas:** Writing – review & editing, Resources, Methodology, Investigation, Funding acquisition, Formal analysis, Conceptualization. **Roberto Estrada:** Methodology, Investigation, Conceptualization. **Mylène de Ruijter:** Writing – review & editing, Investigation, Formal analysis, Conceptualization. **Teodolito Guillén:** Writing – review & editing, Supervision, Resources, Project administration, Methodology, Investigation, Funding acquisition, Formal analysis, Conceptualization.

Declaration of competing interest

The authors declare the following financial interests/personal relationships which may be considered as potential competing interests: Antti Jarvenpaa reports financial support was provided by Business Finland. Teodolito Gullen reports financial support was provided by Tecnológico de Costa Rica. Rafael Vindas reports financial support was provided by National University of Costa Rica School of Veterinary Medicine. If there are other authors, they declare that they have no known competing financial interests or personal relationships that could have appeared to influence the work reported in this paper.

Acknowledgments

The authors acknowledge funding and support from the Future Manufacturing Technologies (FMT) research group at the Kerttu Saalasti Institute, University of Oulu; Business Finland for the DREAMS project; the Research and Extension Vice-rectory of the Costa Rica Institute of Technology and the support provided by the Postgraduate Office for this publication; the School of Veterinary Medicine, Costa Rica National University for in-vivo protocols and experimentation; and the Institutional Laboratory of Microscopy at the Costa Rica Institute of Technology for SEM images.

Data availability

The data that has been used is confidential.

References

[1] S. Alipour, S. Nour, S.M. Attari, M. Mohajeri, S. Kianersi, F. Taromian, M. Khalkhali, G.E. Aninwene, L. Tayebi, A review on *in vitro/in vivo* response of additively manufactured Ti–6Al–4V alloy, J. Mater. Chem. B 10 (2022) 9479–9534, https://doi.org/10.1039/D2TB01616H.

[2] W. Abd-Elaziem, M.A. Darwish, A. Hamada, W.M. Daoush, Titanium-Based alloys and composites for orthopedic implants Applications: a comprehensive review, Mater. Des. 241 (2024) 112850, https://doi.org/10.1016/j.matdes.2024.112850.

[3] A. Ataee, Y. Li, M. Brandt, C. Wen, Ultrahigh-strength titanium gyroid scaffolds manufactured by selective laser melting (SLM) for bone implant applications, Acta Mater. 158 (2018) 354–368, https://doi.org/10.1016/j.actamat.2018.08.005.

[4] L. Zhang, L. Chen, A review on biomedical titanium alloys: recent progress and prospect, Adv. Eng. Mater. 21 (2019), https://doi.org/10.1002/adem.201801215.

[5] A. Ataee, Y. Li, D. Fraser, G. Song, C. Wen, Anisotropic Ti-6Al-4V gyroid scaffolds manufactured by electron beam melting (EBM) for bone implant applications, Mater. Des. 137 (2018) 345–354, https://doi.org/10.1016/j.matdes.2017.10.040.

[6] E. Yang, M. Leary, B. Lozanovski, D. Downing, M. Mazur, A. Sarker, A. Khorasani, A. Jones, T. Maconachie, S. Bateman, M. Easton, M. Qian, P. Choong, M. Brandt, Effect of geometry on the mechanical properties of Ti-6Al-4V Gyroid structures fabricated via SLM: a numerical study, Mater. Des. 184 (2019) 108165, https://doi.org/10.1016/j.matdes.2019.108165.

[7] L.E. Murr, K.N. Amato, S.J. Li, Y.X. Tian, X.Y. Cheng, S.M. Gaytan, E. Martinez, P. W. Shindo, F. Medina, R.B. Wicker, Microstructure and mechanical properties of open-cellular biomaterials prototypes for total knee replacement implants fabricated by electron beam melting, J. Mech. Behav. Biomed. Mater. 4 (2011) 1396–1411, https://doi.org/10.1016/j.jmbbm.2011.05.010.

[8] F. Bartolomeu, M.M. Costa, N. Alves, G. Miranda, F.S. Silva, Selective Laser Melting of Ti6Al4V sub-millimetric cellular structures: prediction of dimensional deviations and mechanical performance, J. Mech. Behav. Biomed. Mater. 113 (2021) 104123, https://doi.org/10.1016/j.jmbbm.2020.104123.

[9] A. Yánez, A. Cuadrado, O. Martel, H. Afonso, D. Monopoli, Gyroid porous titanium structures: a versatile solution to be used as scaffolds in bone defect reconstruction, Mater. Des. 140 (2018) 21–29, https://doi.org/10.1016/j.matdes.2017.11.050.

[10] D. Barba, E. Alabort, R.C. Reed, Synthetic bone: design by additive manufacturing, Acta Biomater. 97 (2019) 637–656, https://doi.org/10.1016/j.actbio.2019.07.049.

[11] F.S.L. Bobbert, K. Lietaert, A.A. Eftekhari, B. Pouran, S.M. Ahmadi, H. Weinans, A. A. Zadpoor, Additively manufactured metallic porous biomaterials based on minimal surfaces: a unique combination of topological, mechanical, and mass transport properties, Acta Biomater. 53 (2017) 572–584, https://doi.org/10.1016/j.actbio.2017.02.024.

[12] F. Günther, S. Pilz, F. Hirsch, M. Wagner, M. Kästner, A. Gebert, M. Zimmermann, Shape optimization of additively manufactured lattices based on triply periodic minimal surfaces, Addit. Manuf. 73 (2023) 103659, https://doi.org/10.1016/j.addma.2023.103659.

[13] F. Günther, F. Hirsch, S. Pilz, M. Wagner, A. Gebert, M. Kästner, M. Zimmermann, Structure-property relationships of imperfect additively manufactured lattices based on triply periodic minimal surfaces, Mater. Des. 222 (2022) 111036, https://doi.org/10.1016/j.matdes.2022.111036.

[14] H. Barber, C.N. Kelly, K. Nelson, K. Gall, Compressive anisotropy of sheet and strut based porous Ti–6Al–4V scaffolds, J. Mech. Behav. Biomed. Mater. 115 (2021) 104243, https://doi.org/10.1016/j.jmbbm.2020.104243.

[15] L. Yang, S. Wu, C. Yan, P. Chen, L. Zhang, C. Han, C. Cai, S. Wen, Y. Zhou, Y. Shi, Fatigue properties of Ti-6Al-4V Gyroid graded lattice structures fabricated by laser powder bed fusion with lateral loading, Addit. Manuf. 46 (2021) 102214, https://doi.org/10.1016/j.addma.2021.102214.

[16] S. Kechagias, R.N. Oosterbeek, M.J. Munford, S. Ghouse, J.R.T. Jeffers, Controlling the mechanical behaviour of stochastic lattice structures: the key role of nodal connectivity, Addit. Manuf. 54 (2022) 102730, https://doi.org/10.1016/j.addma.2022.102730.

[17] S. Ghouse, S. Babu, R.J. Van Arkel, K. Nai, P.A. Hooper, J.R.T. Jeffers, The influence of laser parameters and scanning strategies on the mechanical properties of a stochastic porous material, Mater. Des. 131 (2017) 498–508, https://doi.org/10.1016/j.matdes.2017.06.041.

[18] S. Kanwar, S. Vijayavenkataraman, 3D printable bone-mimicking functionally gradient stochastic scaffolds for tissue engineering and bone implant applications, Mater. Des. 223 (2022) 111199, https://doi.org/10.1016/j.matdes.2022.111199.

[19] A. Cheng, A. Humayun, D.J. Cohen, B.D. Boyan, Z. Schwartz, Additively manufactured 3D porous Ti-6Al-4V constructs mimic trabecular bone structure and regulate osteoblast proliferation, differentiation and local factor production in a porosity and surface roughness dependent manner, Biofabrication 6 (2014) 045007, https://doi.org/10.1088/1758-5082/6/4/045007.

[20] N. Soro, E.G. Brodie, A. Abdal-hay, A.Q. Alali, D. Kent, M.S. Dargusch, Additive manufacturing of biomimetic Titanium-Tantalum lattices for biomedical implant applications, Mater. Des. 218 (2022) 110688, https://doi.org/10.1016/j.matdes.2022.110688.

[21] S.Y. Choy, C.-N. Sun, K.F. Leong, J. Wei, Compressive properties of Ti-6Al-4V lattice structures fabricated by selective laser melting: design, orientation and density, Addit. Manuf. 16 (2017) 213–224, https://doi.org/10.1016/j.addma.2017.06.012.

[22] S.A. Tyagi M M, Additive manufacturing of titanium-based lattice structures for medical applications – a review, Bioprinting 30 (2023) e00267, https://doi.org/10.1016/j.bprint.2023.e00267.

[23] Y. Wu, J. Liu, L. Kang, J. Tian, X. Zhang, J. Hu, Y. Huang, F. Liu, H. Wang, Z. Wu, An overview of 3D printed metal implants in orthopedic applications: present and

future perspectives, Heliyon 9 (2023) e17718, https://doi.org/10.1016/j.heliyon.2023.e17718.
[24] S. Ma, Q. Tang, X. Han, Q. Feng, J. Song, R. Setchi, Y. Liu, Y. Liu, A. Goulas, D. S. Engstrøm, Y.Y. Tse, N. Zhen, Manufacturability, mechanical properties, mass-transport properties and biocompatibility of triply periodic minimal surface (TPMS) porous scaffolds fabricated by selective laser melting, Mater. Des. 195 (2020) 109034, https://doi.org/10.1016/j.matdes.2020.109034.
[25] S. Kumawat, S.R. Deshmukh, R.R. Ghorpade, Fabrication of Ti-6Al-4v cellular lattice structure using selective laser melting for orthopedic use: a review, Mater. Today Proc. (2023), https://doi.org/10.1016/j.matpr.2023.08.053.
[26] A. Benady, S.J. Meyer, E. Golden, S. Dadia, G. Katarivas Levy, Patient-specific Ti-6Al-4V lattice implants for critical-sized load-bearing bone defects reconstruction, Mater. Des. 226 (2023) 111605, https://doi.org/10.1016/j.matdes.2023.111605.
[27] A. Vance, K. Bari, A. Arjunan, Compressive performance of an arbitrary stiffness matched anatomical Ti64 implant manufactured using Direct Metal Laser Sintering, Mater. Des. 160 (2018) 1281–1294, https://doi.org/10.1016/j.matdes.2018.11.005.
[28] J.M. Shum, B.C. Gadomski, S.J. Tredinnick, W. Fok, J. Fernandez, B. Nelson, R. H. Palmer, K.C. McGilvray, G.J. Hooper, C. Puttlitz, J. Easley, T.B.F. Woodfield, Enhanced bone formation in locally-optimised, low-stiffness additive manufactured titanium implants: an in silico and in vivo tibial advancement study, Acta Biomater. 156 (2023) 202–213, https://doi.org/10.1016/j.actbio.2022.04.006.
[29] M. Geetha, A.K. Singh, R. Asokamani, A.K. Gogia, Ti based biomaterials, the ultimate choice for orthopaedic implants – a review, Prog. Mater. Sci. 54 (2009) 397–425, https://doi.org/10.1016/j.pmatsci.2008.06.004.
[30] Y. Zhang, J. Li, S. Che, Z. Yang, Y. Tian, Chemical leveling mechanism and oxide film properties of additively manufactured Ti–6Al–4V alloy, J. Mater. Sci. 54 (2019) 13753–13766, https://doi.org/10.1007/s10853-019-03855-4.
[31] S.M. Cokelaere, R.A. Vindas Bolaños, S.K. Both, M. Vullers, N.M. Korthagen, P. R. van Weeren, J.C. de Grauw, Nanofracturing: a new technique for bone marrow stimulation in equine cartilage repair, Pferdeheilkunde Equine Medicine 36 (2020) 100–106, https://doi.org/10.21836/PEM20200201, 100–106.
[32] R.A. Vindas Bolaños, S.M. Cokelaere, J.M. Estrada McDermott, K.E.M. Benders, U. Gbureck, S.G.M. Plomp, H. Weinans, J. Groll, P.R. van Weeren, J. Malda, The use of a cartilage decellularized matrix scaffold for the repair of osteochondral defects: the importance of long-term studies in a large animal model, Osteoarthritis Cartilage 25 (2017) 413–420, https://doi.org/10.1016/j.joca.2016.08.005.
[33] R.V. Bolaños, M. Castilho, J. de Grauw, S. Cokelaere, S. Plomp, J. Groll, P.R. van Weeren, U. Gbureck, J. Malda, Long-term in vivo performance of low-temperature 3D-printed bioceramics in an equine model, ACS Biomater. Sci. Eng. 6 (2020) 1681–1689, https://doi.org/10.1021/acsbiomaterials.9b01819.
[34] P. Diloksumpan, R.V. Bolaños, S. Cokelaere, B. Pouran, J. de Grauw, M. van Rijen, R. van Weeren, R. Levato, J. Malda, Orthotopic bone regeneration within 3D printed bioceramic scaffolds with region-dependent porosity gradients in an equine model, Adv. Healthcare Mater. 9 (2020), https://doi.org/10.1002/adhm.201901807.
[35] D. Zhao, H. Liang, C. Han, J. Li, J. Liu, K. Zhou, C. Yang, Q. Wei, 3D printing of a titanium-tantalum Gyroid scaffold with superb elastic admissible strain, bioactivity and in-situ bone regeneration capability, Addit. Manuf. 47 (2021) 102223, https://doi.org/10.1016/j.addma.2021.102223.
[36] X. Yuan, Y. Kang, J. Zuo, Y. Xie, L. Ma, X. Ren, Z. Bian, Q. Wei, K. Zhou, X. Wang, Z. Yu, Micro/nano hierarchical structured titanium treated by NH4OH/H2O2 for enhancing cell response, PLoS One 13 (2018) e0196366, https://doi.org/10.1371/journal.pone.0196366.
[37] D. Nazarov, E. Zemtsova, V. Smirnov, I. Mitrofanov, M. Maximov, N. Yudintceva, M. Shevtsov, The effects of chemical etching and ultra-fine grain structure of titanium on MG-63 cells response, Metals 11 (2021) 510, https://doi.org/10.3390/met11030510.
[38] D.V. Nazarov, V.M. Smirnov, E.G. Zemtsova, N.M. Yudintceva, M.A. Shevtsov, R. Z. Valiev, Enhanced osseointegrative properties of ultra-fine-grained titanium implants modified by chemical etching and atomic layer deposition, ACS Biomater. Sci. Eng. 4 (2018) 3268–3281, https://doi.org/10.1021/acsbiomaterials.8b00342.
[39] Q. Sun, J. Sun, K. Guo, L. Wang, Compressive mechanical properties and energy absorption characteristics of SLM fabricated Ti6Al4V triply periodic minimal surface cellular structures, Mech. Mater. 166 (2022) 104241, https://doi.org/10.1016/j.mechmat.2022.104241.
[40] L. Yang, R. Mertens, M. Ferrucci, C. Yan, Y. Shi, S. Yang, Continuous graded Gyroid cellular structures fabricated by selective laser melting: design, manufacturing and mechanical properties, Mater. Des. 162 (2019) 394–404, https://doi.org/10.1016/j.matdes.2018.12.007.
[41] D.K. Pattanayak, A. Fukuda, T. Matsushita, M. Takemoto, S. Fujibayashi, K. Sasaki, N. Nishida, T. Nakamura, T. Kokubo, Bioactive Ti metal analogous to human cancellous bone: fabrication by selective laser melting and chemical treatments, Acta Biomater. 7 (2011) 1398–1406, https://doi.org/10.1016/j.actbio.2010.09.034.
[42] B. Van Hooreweder, Y. Apers, K. Lietaert, J.-P. Kruth, Improving the fatigue performance of porous metallic biomaterials produced by Selective Laser Melting, Acta Biomater. 47 (2017) 193–202, https://doi.org/10.1016/j.actbio.2016.10.005.
[43] Y.Y. Sun, S.L. Lu, S. Gulizia, C.H. Oh, D. Fraser, M. Leary, M. Qian, Fatigue performance of additively manufactured Ti-6Al-4V: surface condition vs. Internal defects, JOM 72 (2020) 1022–1030, https://doi.org/10.1007/s11837-020-04025-7.
[44] B. Ren, Y. Wan, C. Liu, H. Wang, M. Yu, X. Zhang, Y. Huang, Improved osseointegration of 3D printed Ti-6Al-4V implant with a hierarchical micro/nano surface topography: an in vitro and in vivo study, Mater. Sci. Eng. C 118 (2021) 111505, https://doi.org/10.1016/j.msec.2020.111505.
[45] N. Wang, G.K. Meenashisundaram, D. Kandilya, J.Y.H. Fuh, S.T. Dheen, A. S. Kumar, A biomechanical evaluation on Cubic, Octet, and TPMS gyroid Ti6Al4V lattice structures fabricated by selective laser melting and the effects of their debris on human osteoblast-like cells, Biomater. Adv. 137 (2022) 212829, https://doi.org/10.1016/j.bioadv.2022.212829.
[46] C.N. Kelly, J. Francovich, S. Julmi, D. Safranski, R.E. Guldberg, H.J. Maier, K. Gall, Fatigue behavior of As-built selective laser melted titanium scaffolds with sheet-based gyroid microarchitecture for bone tissue engineering, Acta Biomater. 94 (2019) 610–626, https://doi.org/10.1016/j.actbio.2019.05.046.
[47] G. Yu, X. Li, L. Dai, L. Xiao, W. Song, Compressive properties of imperfect Ti-6Al-4V lattice structure fabricated by electron beam powder bed fusion under static and dynamic loadings, Addit. Manuf. 49 (2022) 102497, https://doi.org/10.1016/j.addma.2021.102497.
[48] L. Bai, J. Zhang, X. Chen, C. Yi, R. Chen, Z. Zhang, Configuration optimization design of Ti6Al4V lattice structure formed by SLM, Materials 11 (2018) 1856, https://doi.org/10.3390/ma11101856.
[49] L.J. Gibson, Biomechanics of cellular solids, J. Biomech. 38 (2005) 377–399, https://doi.org/10.1016/j.jbiomech.2004.09.027.
[50] B. Hanks, J. Berthel, M. Frecker, T.W. Simpson, Mechanical properties of additively manufactured metal lattice structures: data review and design interface, Addit. Manuf. 35 (2020) 101301, https://doi.org/10.1016/j.addma.2020.101301.
[51] C. Zhang, H. Qiao, L. Yang, W. Ouyang, T. He, B. Liu, X. Chen, N. Wang, C. Yan, Vibration characteristics of additive manufactured IWP-type TPMS lattice structures, Compos. Struct. 327 (2024) 117642, https://doi.org/10.1016/j.compstruct.2023.117642.
[52] S. Frosch, V. Nüsse, K.-H. Frosch, W. Lehmann, G. Buchhorn, Osseointegration of 3D porous and solid Ti–6Al–4V implants - narrow gap push-out testing and experimental setup considerations, J. Mech. Behav. Biomed. Mater. 115 (2021) 104282, https://doi.org/10.1016/j.jmbbm.2020.104282.
[53] Y.-T. Wang, C.-M. Chang, P.-H. Liu, C.-L. Lin, Feasibility evaluation of a new lattice for porous surface design in additive manufacturing medical implants under interfacial tensile bonded testing, Addit. Manuf. 66 (2023) 103455, https://doi.org/10.1016/j.addma.2023.103455.
[54] Á.É. Kovács, Z. Csernátony, L. Csámer, G. Méhes, D. Szabó, M. Veres, M. Braun, B. Harangi, N. Serbán, L. Zhang, G. Falk, H. Soósné Horváth, S. Manó, Comparative analysis of bone ingrowth in 3D-printed titanium lattice structures with different patterns, Materials 16 (2023) 3861, https://doi.org/10.3390/ma16103861.
[55] G. Zhang, P. Zhao, L. Lin, L. Qin, Z. Huan, S. Leeflang, A.A. Zadpoor, J. Zhou, L. Wu, Surface-treated 3D printed Ti-6Al-4V scaffolds with enhanced bone regeneration performance: an in vivo study, Ann. Transl. Med. 9 (2021), https://doi.org/10.21037/atm-20-3829, 39–39.
[56] A.-F. Obaton, J. Fain, D. Meinel, A. Tsamos, F. Léonard, B. Lécuelle, M. Djemaï, In vivo bone progression in and around lattice implants additively manufactured with a new titanium alloy, Appl. Sci. 13 (2023) 7282, https://doi.org/10.3390/app13127282.